

1 **Gravity wave induced instability of the stratospheric polar vortex edge**

2 Lawrence Coy,^{a,b} Paul A. Newman,^a William M. Putman,^a Steven Pawson,^a and
3 M. Joan Alexander^c

4 ^a*NASA GSFC, Greenbelt, MD, USA*

5 ^b*SSAI, Lanham, MD, USA*

6 ^c*NWRA, Boulder, CO, USA*

7 *Corresponding author:* Lawrence Coy, lawrence.coy@nasa.gov

8 ABSTRACT: We report on a previously undocumented process capable of mixing Northern Hemi-
9 sphere (NH) winter Ertel potential vorticity (EPV)—instabilities introduced along the stratospheric
10 polar vortex edge by breaking gravity waves (GWs). As horizontal resolution has increased, global
11 scale atmospheric models and data assimilation systems (DAS) are now able to capture some
12 aspects of GW generation, propagation, and dissipation, as well as mesoscale EPV disturbances.
13 This work examines resolved GWs, their breaking, and their interaction with the stratospheric polar
14 vortex as seen in the NASA Global Modeling and Assimilation Office DAS during the 2021–2022
15 NH winter. This analysis shows that tropospheric generated GWs, breaking in the stratosphere
16 over a substantial area, created a significant disruption of the polar vortex EPV, in turn trigger-
17 ing baroclinic instabilities near the edge of the polar vortex. The instabilities take the form of
18 mesoscale vortices propagating on the edge of the stratospheric polar vortex. This work reveals
19 two new features in the EPV analysis: high and low fluctuations at the smallest model scale created
20 by resolved GW breaking, and high values associated with mesoscale vortices along the edge of
21 the polar vortex.

22 **1. Introduction**

23 Past studies of the stratosphere have emphasized the importance of Ertel’s potential vorticity
24 (EPV) as a well conserved dynamical tracer (Hoskins et al. 1985). These early studies often
25 dealt with limited horizontal resolution making the identification of important global EPV features
26 remarkable at the time. For Example, McIntyre and Palmer (1983) characterized the EPV fields
27 used in their discovery of breaking planetary waves as “. . . resembling a blurred view of reality seen
28 through a pane of knobbly glass . . .”. This “knobbly glass” has been smoothed considerably over
29 the following decades based on data assimilation techniques in conjunction with high horizontal
30 resolution global models. Indeed, recent data assimilation reanalysis of the McIntyre and Palmer
31 (1983) breaking wave examples provides dynamically consistent confirmations of their breaking
32 planetary wave discovery (Butchart 2022).

33 While the planetary scale waves are well resolved in modern EPV fields, the question arises
34 as to the possibility of increased model resolution leading to new discoveries. That is, can
35 “magnification” of current EPV fields provide further insights into stratosphere and mesosphere
36 dynamics. Here we investigate two new features resulting from increased horizontal resolution:
37 signatures of breaking gravity waves (GW) followed by the formation of mesoscale vortices on the
38 polar vortex edge.

39 The Northern Hemisphere (NH) stratospheric polar vortex forms every winter, however, consid-
40 erable vortex variability exists, especially in years with stratospheric sudden warmings (SSWs).
41 During SSW events, high Ertel potential vorticity (EPV) in the stratospheric polar vortex is mixed
42 down to lower latitudes by global-scale planetary waves. The planetary waves are said to be
43 “breaking” when they create regions where the latitudinal EPV gradient is reversed and these
44 reversed gradient regions can lead to instabilities in the wave breaking region (see Butchart 2022,
45 and references therein).

46 Here we report on another process capable of mixing NH winter EPV—instabilities introduced
47 along the polar vortex edge by breaking gravity waves (GW). GWs are generated by flow over
48 orography, convection, fronts, or flow instabilities (Alexander 2010). Their successful vertical
49 propagation depends on the background atmospheric flow. Under the right conditions GWs can
50 transfer significant momentum and energy from the troposphere to the middle atmosphere. As
51 vertically propagating GWs encounter lower densities or approach a critical layer, they increase

52 in amplitude until they become unstable and "break", depositing momentum and energy to the
53 background flow and hence providing the possibility of disrupting the winter stratospheric polar
54 vortex.

55 As noted above, global scale atmospheric models and data assimilation systems (DAS) routinely
56 resolve the main features of the stratospheric polar vortex along with planetary wave variability
57 and breaking. As the horizontal resolution has increased over time these models are now able
58 to capture convective systems and some aspects of GW generation, propagation, and dissipation
59 (Holt et al. 2017; Stevens et al. 2019; Shibuya and Sato 2019; Okui et al. 2023). Here we report on
60 resolved GWs, their breaking, and their interaction with the stratospheric polar vortex as seen in
61 the NASA Global Modeling and Assimilation Office (GMAO) near real time forward processing
62 (FP) system during the 2021–2022 NH winter.

63 Our plan is to examine a somewhat atypical NH winter (2021–2022), where planetary wave
64 activity was relatively weak and the stratospheric polar vortex strong, allowing GWs to dominate
65 the polar vortex disturbances. The working hypothesis is that orographically generated GWs,
66 breaking in the mid-to upper stratosphere, distorted the edge of the polar vortex, creating regions
67 of unstable EPV gradients. These in turn generated a series of what will be called here mesoscale
68 vortices, incorporating signatures of latitudinal mixing, on the edge of the polar vortex.

69 As will be shown below, the mesoscale vortices generated by the breaking gravity waves de-
70 veloped centers with extremely high EPV. While EPV is often well conserved in the stratosphere
71 (Haynes and McIntyre 1990), diabatic and frictional forces can change the EPV of an air parcel
72 (Haynes and McIntyre 1987) and such non-conservation processes must be occurring here. The
73 development and propagation of the high EPV mesoscale vortices will be documented below,
74 however, a detailed EPV budget is left for future studies.

75 In the following, Section 2 provides a description of the DA systems and models used. The
76 main DAS is the NASA GEOS (Global Earth Observing System) FP system, however some lower
77 horizontal resolution MERRA-2 (Modern-Era Retrospective analysis for Research and Applica-
78 tions) output is included for comparison. To investigate the potential for baroclinic instability near
79 the polar vortex edge, results are presented from a linear quasi-geostrophic beta plane model, also
80 described in Section 2. The results are presented in Section 3, with subsections on the 2021-2022
81 NH winter, the resolved GWs, the structure of the mesoscale vortices, dependence on resolution,

82 and the linear instability model. A summary of the results along with conclusions are presented in
83 Section 4.

84 **2. Global Assimilation Products and Data**

85 *a. GEOS FP System*

86 The NASA GMAO GEOS FP DAS routinely produces global, near-real-time, meteorological
87 analysis fields and forecasts available at three hourly intervals. This system updates frequently
88 (approximately every six months) to better incorporate new data types and the latest model de-
89 velopments. The DAS utilizes a full suite of observation types including aerosol, temperature,
90 pressure, radiances, winds, moisture, radio occultation, and ozone measurements. Each six hourly
91 analysis assimilates roughly two million observations. Zhu et al. (2022) provides a current descrip-
92 tion of the GEOS DAS.

93 The system used during the NH winter of 2021–2022 was run at 12 km horizontal resolution on a
94 cubed sphere grid (Putman and Lin 2007) with meteorological fields saved on a 5/16 by 1/4 degree
95 longitude by latitude horizontal grid and on either the full 72 model levels (model top at 0.01 hPa)
96 or vertically interpolated to 42 pressure levels. A description of the model physics can be found
97 in Arnold et al. (2020). The most recent two weeks of forecasts are available on the NASA Center
98 for Climate Simulation (NCCS) data portal. The specific archived analysis fields used in the study
99 are available as described in the Open Research Section.

100 To investigate the dependence on horizontal resolution, EPV fields are shown from a test DAS
101 (x0048) run at half the GEOS FP system resolution (24 km). While the GEOS FP ($\sim 1/8$ degree)
102 and the test system ($\sim 1/4$ degree) are run with different horizontal resolutions, the results are saved
103 on the same output grid.

104 *b. MERRA-2*

105 The MERRA-2 system provides ongoing global atmospheric reanalyses starting in 1980. Unlike
106 the FP system, the MERRA-2 system is frozen, with only the input data changing with time. The
107 MERRA-2 vertical levels are the same as in FP, however MERRA-2, with fields saved at 5/8 by
108 1/2 degree longitude by latitude, has more coarse horizontal resolution than FP. An overview of
109 MERRA-2 is given by Gelaro et al. (2017). Here we used the monthly averaged pressure level

110 fields (GMAO 2015b) when comparing the NH winter 2022 climate with other winters and the
 111 instantaneous model level EPV fields (GMAO 2015a) when comparing specific time EPV fields
 112 between FP and MERRA-2.

113 *c. Linear Instability Model*

114 The potential for baroclinic instability near the disturbed vortex edge is investigated using a
 115 quasi-geostrophic, beta-plane, linear instability model. This is the same model used and described
 116 in McCormack et al. (2014) and is based on the adiabatic and frictionless, linearized potential
 117 vorticity equation (see Andrews et al. 1987, equation 3.4.5 and following equations):

$$q'_t + \bar{u}q'_x + v'\bar{q}_y = 0. \quad (1)$$

118 where q is potential vorticity, u and v are the longitudinal and meridional velocity components,
 119 and x, y, t , are the longitudinal and meridional directions and time. The overbars denote a zonal
 120 average and the primes the deviation from a zonal average. Since q' and v' depend linearly on
 121 the geostrophic stream function, ψ , assuming a wave solution for ψ with phase speed c and zonal
 122 wavenumber k allows the x and t derivatives to be evaluated. With \bar{u} and \bar{q}_y then specified as
 123 the environment to be tested for instability, and suitable boundary conditions, Eq. 1 can be finite
 124 differenced for a chosen value of k as:

$$\mathbf{A}\psi = c\mathbf{B}\psi \quad (2)$$

125 where the matrix, \mathbf{A} , depends on \bar{u} and \bar{q}_y , the matrix, \mathbf{B} , depends on the Laplacian operator, and
 126 ψ is the vector of stream function values at each point in the two dimensional, latitude and altitude,
 127 domain being investigated.

128 Eq. 2, can be solved for ψ and c , using standard routines. For simplicity we assume that the
 129 instability is located far enough from the latitude and altitude domain boundaries that we can take ψ
 130 equal to zero on all boundaries. Examination of the imaginary part of c allows for the identification
 131 of the fastest growing mode structure, ψ , for each value of k specified.

132 *d. AIRS data*

133 For confirmation of the DAS resolved GWs we examined the GW signature found in the AIRS
134 (Atmospheric Infrared Sounder on the NASA Aqua satellite) $4.3 \mu\text{m}$ brightness temperature signal.
135 Horizontal resolution is 13.5 km at the nadir point below the satellite, similar to the resolution
136 of the FP system, and resolution decreases toward the measurement swath edges so that the
137 average resolution is ~ 20 km. The data are low-noise multi-channel averages with weighting
138 functions that peak between 30–40 km altitude (Hoffmann et al. 2014). Brightness temperature
139 wave anomalies are attenuated relative to sensible temperature anomalies, with attenuation that
140 is inversely proportional to vertical wavelength. These channels are most sensitive to the longer
141 vertical wavelength (≥ 15 km) GWs and are not expected to highlight wave breaking regions where
142 the vertical wavelength decreases. Note also that selected AIRS channels are assimilated in the
143 DAS so that the AIRS observations shown here are not entirely independent of the data assimilation
144 output, nevertheless, the AIRS observations shown here can be regarded as an independent analysis
145 of the GWs in the FP system forecasts.

146 **3. Results**

147 *a. The 2021–2022 Northern Hemisphere Winter Stratosphere*

148 The zonal mean of the zonal wind component at 10 hPa, 60°N provides a useful measure of
149 polar vortex strength that can be used to characterize the NH winter stratosphere. Winters with
150 high seasonally averaged DJF (December, January, February) winds either lack SSWs or have them
151 occurring late in the winter season. The 2021–2022 NH winter had the largest mean seasonal wind
152 seen in the 1980–2023 MERRA-2 time period, with a mean seasonal wind of 46.3 ms^{-1} , more than
153 1.5 standard deviations above the average value of 30.3 ms^{-1} .

154 As with the winds, the planetary-scale wave forcing from the troposphere can be considered over
155 the DJF season and variability is expected depending on interannual tropospheric variability. Here
156 we consider the zonally averaged meridional heat flux at 100 hPa and 60°N as a measure of the wave
157 forcing of the stratosphere. The NH 2021–2022 winter season had the lowest meridional heat flux
158 seen in the 1980–2023 MERRA-2 time period, with a mean seasonal heat flux of 17.2 Kms^{-1} , more
159 than 2 standard deviations below the average value of 24.3 Kms^{-1} . The record low 2021–2022
160 planetary-scale wave forcing at 100 hPa and 60°N is consistent with the strong stratospheric winds.

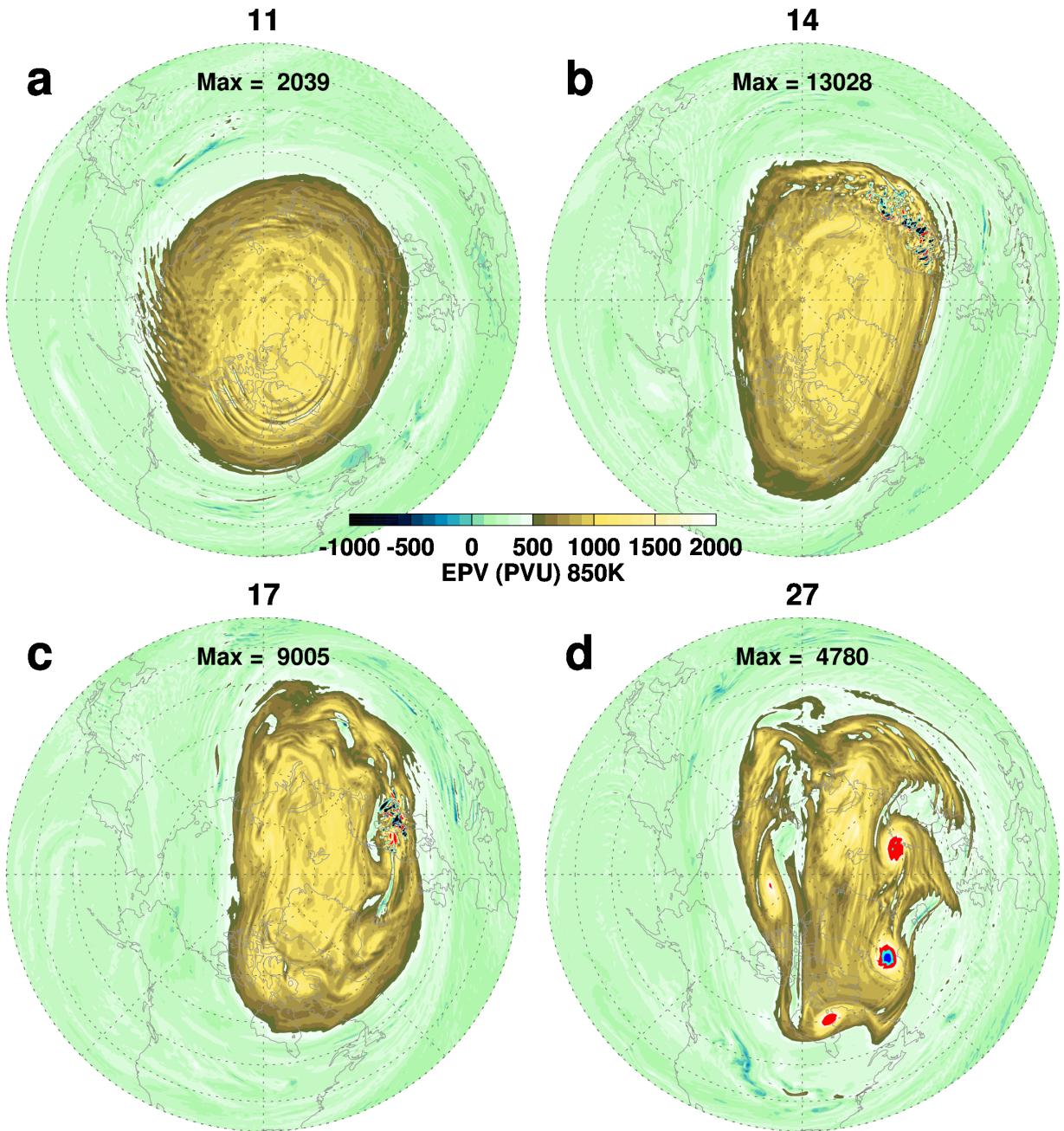
161 The strong winds and low wave forcing conjure up a picture of an undisturbed zonally symmetry
162 polar vortex. Nevertheless, the January 2022 stratospheric polar vortex transformed from a zonally
163 symmetric high Ertel potential vorticity (EPV) configuration (Fig. 1a) on 11 January to a much
164 more disturbed vortex (Fig. 1d) on 27 January. While there is an overall elongation of the 27 January
165 high EPV region, the most striking features are the ragged edge of the vortex (the high EPV region)
166 and the existence of four very high, localized EPV mesoscale vortices along the polar vortex edge.
167 On 11 January the maximum 850K EPV was $\sim 2,000$ PVU while by 27 January the maximum had
168 more than doubled to 4,780 PVU with the highest values associated with the strong EPV mesoscale
169 vortex at 45°W .

174 *b. Resolved gravity waves*

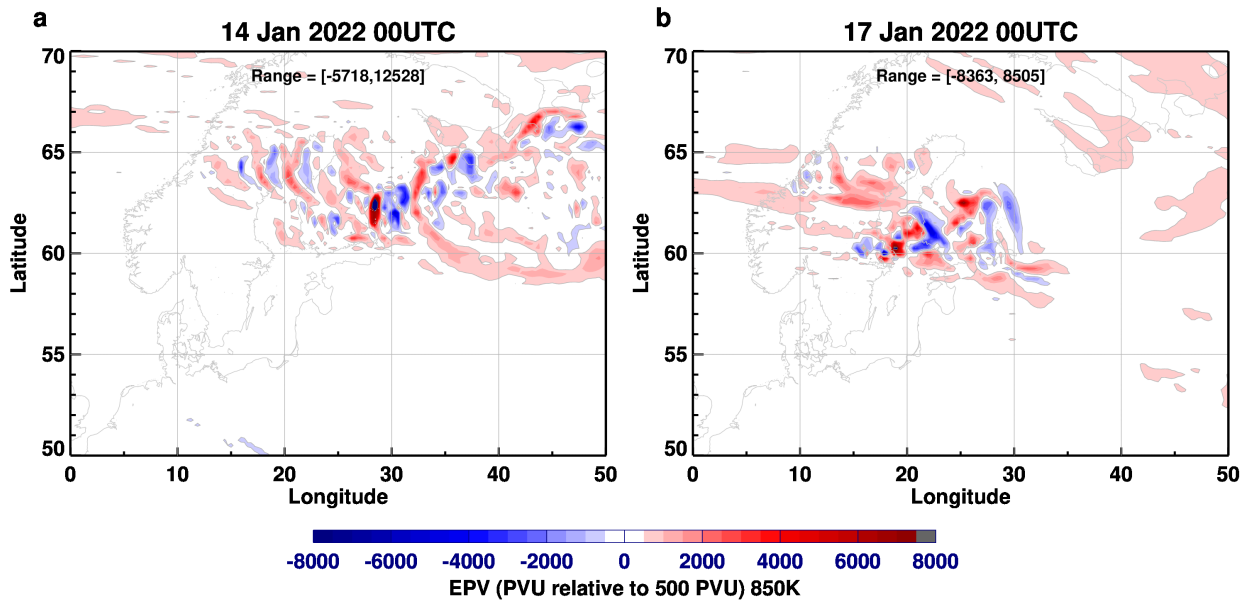
175 Between 11 and 27 January 2022 small regions of extremely high and low EPV values occurred
176 along the vortex edge, especially over Northern Europe with a maximum value of over 13,000 PVU
177 on 14 January (Fig. 1b). The polar vortex edge distorted in response to these perturbations, creating
178 separation of the high EPV from the main vortex on 14 January from 0° – 135°E . By 17 January,
179 the vortex edge became even more distorted as the high and low EPV perturbations continued
180 occurring over Northern Europe (Fig. 1c).

181 Looking more closely at the 850K EPV on 14 and 17 January (Fig. 2), alternating regions of
182 high and low EPV are seen near the polar vortex edge. The EPV values at these times are as much
183 as 8,000 PVU below and 12,500 PVU above the polar vortex edge value. On the 14th (Fig. 2a) a
184 high EPV feature is seen equatorward and then east of the disturbance region corresponding to the
185 EPV filament identified in Fig. 1b.

189 That these small-scale EPV disturbances are related to resolved GWs can be seen in the undu-
190 lations in the height of the 850K potential temperature surface (Fig. 3). The GWs in the height
191 field do not disturb the entire EPV field, as non-dissipating GWs should not be visible in the EPV
192 field, however, the EPV field is disturbed in the more northern part of the GW field where the GWs
193 are likely breaking in a non-EPV conserving manner. Note that the EPV varies on a smaller scale
194 than the scale of the GWs seen in the potential temperature surface oscillations and furthermore
195 that the orientation of the EPV oscillations differs from the orientation of the GWs. This relation
196 between the GW signature and the scale and orientation of the small-scale EPV field is consistent



170 FIG. 1. EPV on the 850K potential temperature surface for a) 11, b) 14, c) 17 and d) 27 January 2022 in
 171 potential vorticity units (PVU) where one PVU is equal to $10^{-6}m^2s^{-1}Kkg^{-1}$. The high EPV values are: red:
 172 2000–3000 PVU, cyan: 3000–4000 PVU, blue: 4000–5000 PVU, and yellow: above 5000 PVU. The vortex edge
 173 on 11 January 2022 is located at 500 PVU based on the method of Nash et al. (1996).

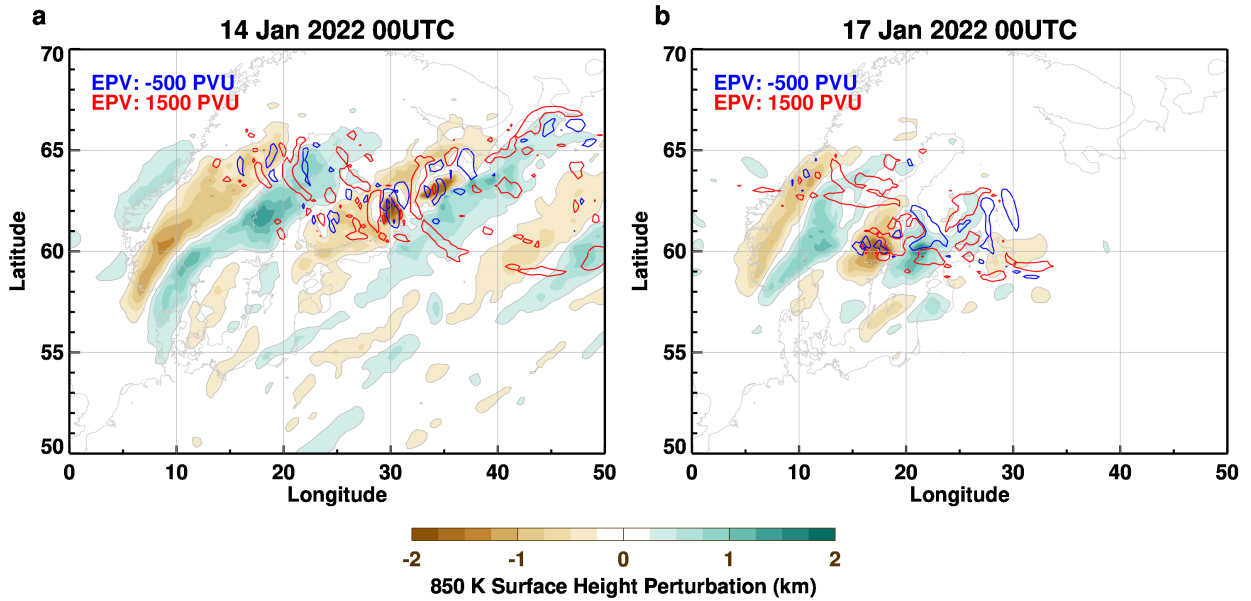


186 FIG. 2. Latitude (50-70°N) longitude (0°-50°E) projection of EPV on the 850K potential temperature surface
 187 for a) 14 January 2022 and b) 17 January 2022. The EPV contours are relative to 500 PVU, the value defining
 188 the vortex edge on 11 January 2022.

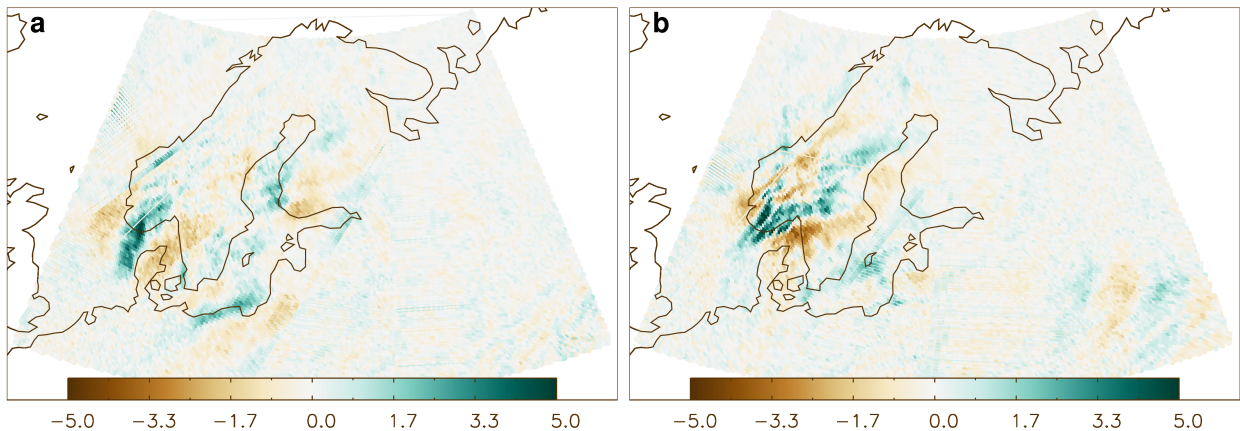
197 with detailed 3D model studies of GW breaking and with GW observations (Fritts and Alexander
 198 2003, and references therein).

202 These model resolved GWs can also be seen directly in the AIRS observations (Fig. 4). These
 203 wave patterns highlight regions over southern Scandinavia where the strong GWs have the largest
 204 vertical wavelengths. Note that these brightness temperatures correspond well with the regions
 205 of potential temperature height surface variations shown in Fig. 3. In the regions where EPV
 206 fluctuations are large the AIRS GW signal is weak. This is more evidence that the EPV fluctuations
 207 characterize regions where GWs are breaking and hence have small vertical wavelengths there.

212 The vertical cross sections of potential temperature and zonal wind on 14 and 17 January (Fig. 5)
 213 highlight the stratospheric breaking wave region, topped by the strong easterly vertical wind shear
 214 and reversal of the zonal wind direction near the stratopause that inhibits the vertical propagation
 215 of orographic GWs. Thus the GWs are required to break in the stratosphere at this time. On both
 216 the 14th and the 17th the strong stratospheric westerlies at 10°W are reduced after crossing the GW
 217 region and are much weaker by 50°E, an indication that the wave breaking may be reducing the
 218 zonal wind. Nearly vertical potential temperature surfaces are also found on both the 14th and 17th

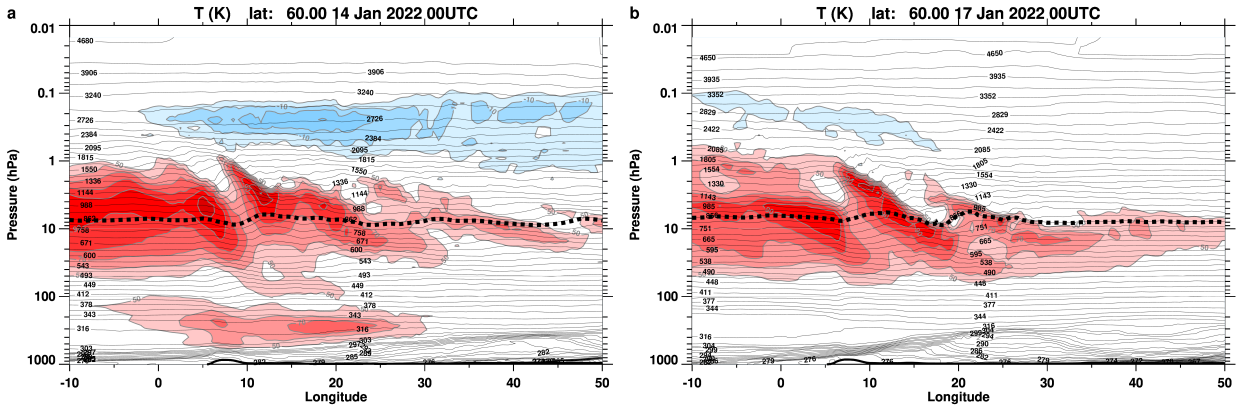


199 FIG. 3. Latitude (50-70°N) longitude (0°W-50°E) projection of the height of the 850K potential temperature
 200 surface (filled contours) and the -500 (blue) and 1500 (red) PVU contours on a) 14 January 2022 and b) 17
 201 January 2022.



208 FIG. 4. AIRS 4.3 μm brightness temperature anomalies on descending (nighttime) overpasses on a) 14 January
 209 and b) 17 January showing large amplitude mountain waves over southern Scandinavia. The UT times listed
 210 are the overpass times that cover the mountain waves. These are low-noise multi-channel averages described in
 211 Hoffmann et al. (2014) with weighting functions that peak between 30-40 km altitude.

219 (Fig. 5) indicating breaking gravity waves at 60°N and likely at nearby latitudes as well, including
 220 the 60-65°N regions of small scale EPV features seen in Fig. 3.



221 FIG. 5. Longitude (10°W–50°E) altitude (1000–0.01 hPa) cross section at 60°N of potential temperature (gray
 222 contours) and zonal wind (filled contours). The dotted black curve denotes the 850K potential temperature
 223 surface. The contour interval for the zonal field is 10 ms⁻¹ and only winds great than 50 ms⁻¹ (red shades) and
 224 less than 0 ms⁻¹ (blue shades) are shown.

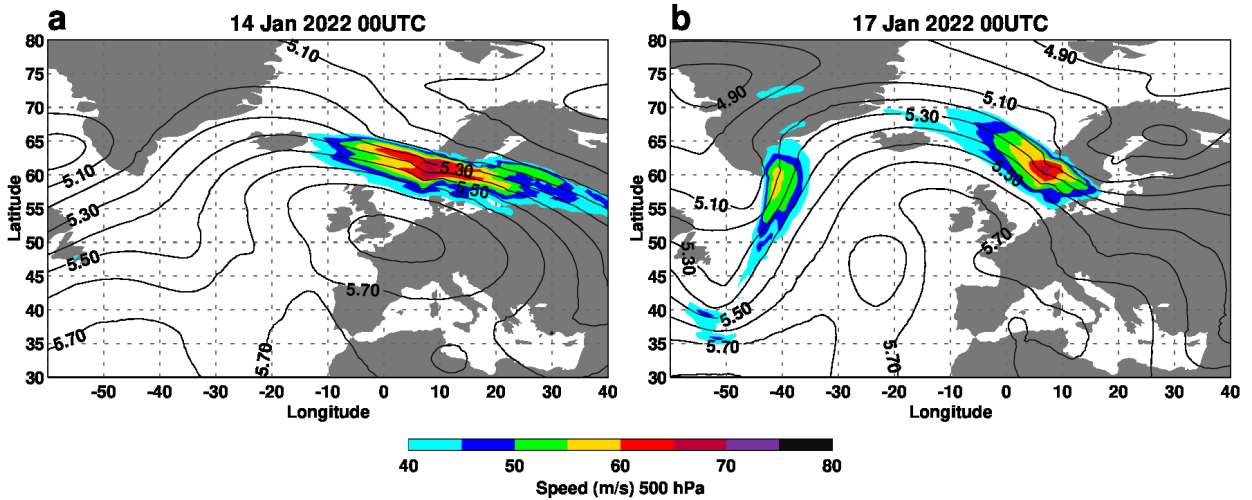
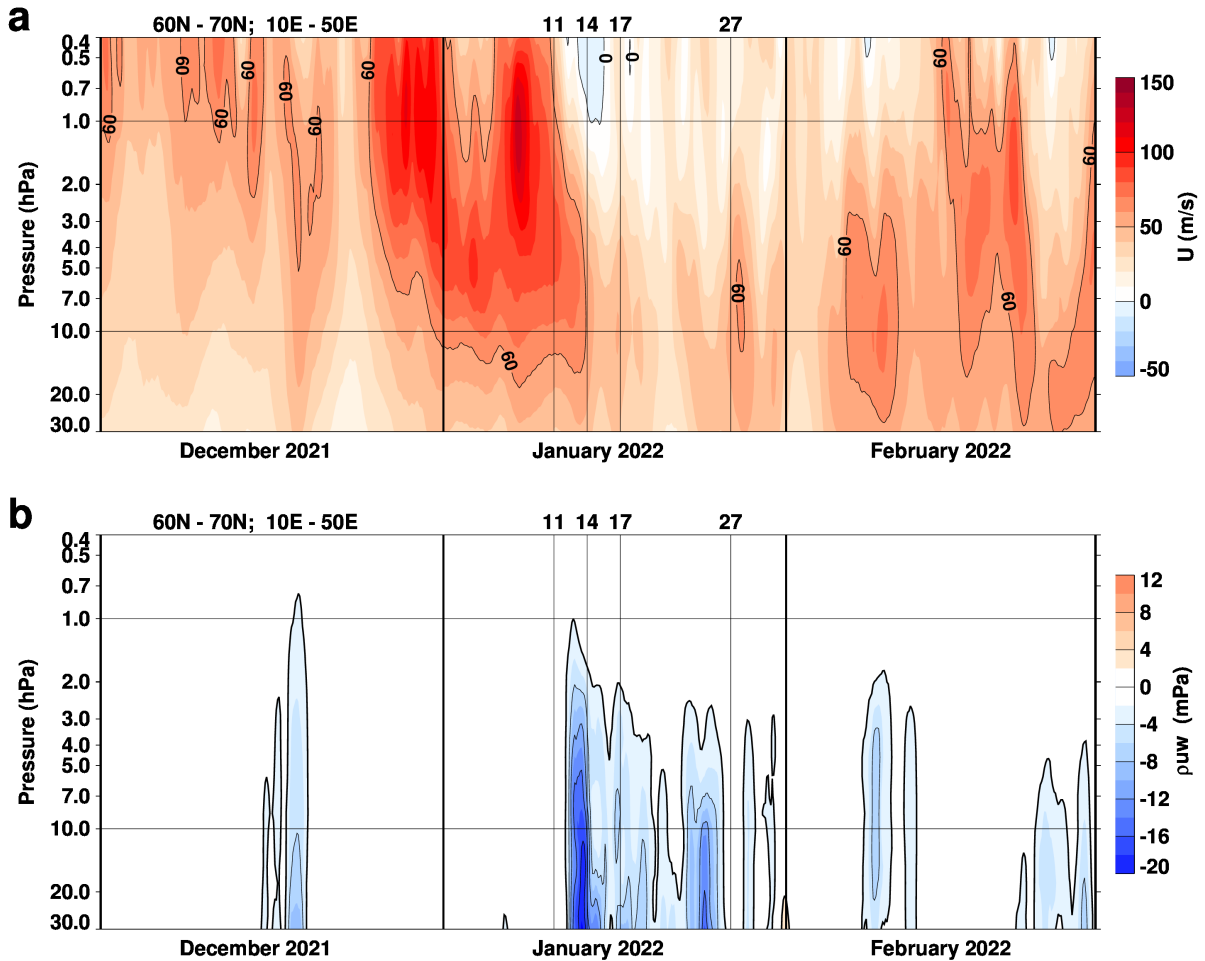


FIG. 6. Wind speed and geopotential heights at 500 hPa for a) 14 January 2022 and b) 17 January 2022.

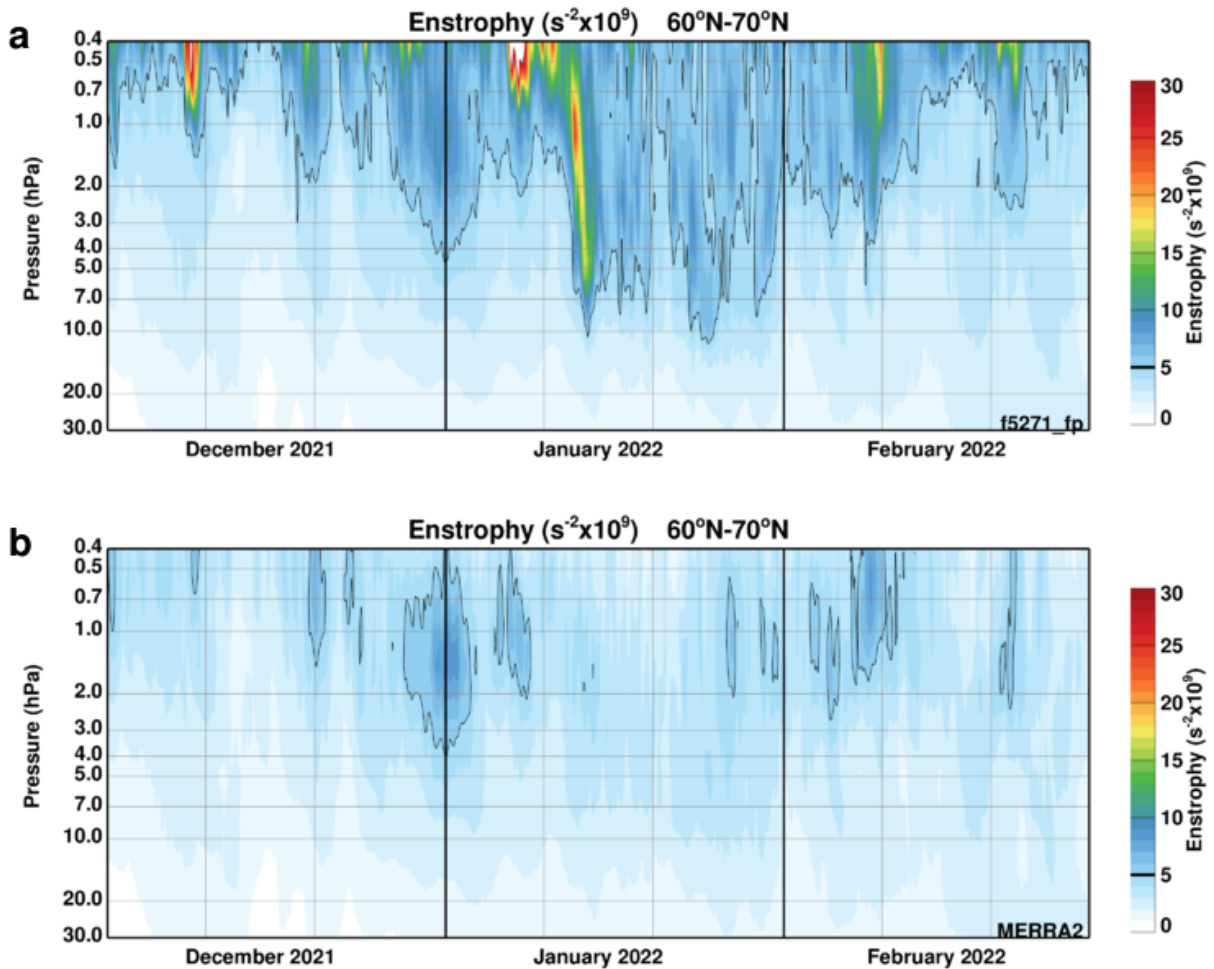
225 These relatively large amplitude GWs in the stratosphere were generated by strong tropospheric
 226 northwesterly winds over Scandinavia (Fig. 6). The synoptic weather situation at this time was
 227 ideal for GW generation with a large, upper-air, high pressure system just west of the European
 228 orography. The westerly wind component in both the troposphere and stratosphere allowed wave
 229 propagation into the upper stratosphere.



236 FIG. 7. Time (DJF) pressure (30–10 hPa) cross sections averaged over 60°–70°N and 10°–50°E for a) zonal
 237 mean zonal wind (ms^{-1}) and b) the zonal component of the density weighted vertical momentum flux (mPa).

230 While the 60°N zonal wind during 2021–22 was relatively strong, it did weaken during January
 231 2022, especially over the breaking gravity wave region (Fig. 7a). This weakening of the zonal wind
 232 after 11 January corresponds to the time of the peak vertical momentum flux over Europe (Fig. 7b).
 233 These strong vertical momentum fluxes are characteristic of GWs. Note that this momentum flux
 234 is greatest in the upper stratosphere and weakens above 1 hPa in the mesosphere, consistent with
 235 the GW wave structure shown in Fig. 5.

238 The small scale GWs and mesoscale vortices as seen in Fig. 1d can be identified by the occurrence
 239 of high values of enstrophy, the square of the vorticity (Fig. 8a). There is a January 2022 burst of
 240 enstrophy coincident with the strong vertical momentum flux and these upper stratospheric strong



247 FIG. 8. Time (DJF) pressure (30–10 hPa) zonal averages of enstrophy ($s^{-2} \times 10^6$) over 60–70°N for a) the
 248 GMAO NRT system and b) MERRA-2.

241 enstrophy values continue to the end of January created by both continued GW activity and the
 242 development of the mesoscale vortices. MERRA-2 lacks the higher horizontal resolution of the
 243 NRT system, hence the small scale features seen in the NRT system's enstrophy (Fig. 8a) are not
 244 seen in MERRA-2 (Fig. 8b). MERRA-2 captures some of the mesoscale vortices as seen by the
 245 slightly high than average enstrophy values during the last third of January at 10 hPa, however, it
 246 misses the very strong enstrophy values characteristic of GW breaking near mid-January.

249 Note that the identification of breaking GW regions with small-scale, large positive and negative
 250 EPV fluctuations, does not imply that these are being realistically modeled as the scale of the
 251 fluctuations is near the limit of the model resolution. Rather they are taken here as a signature of

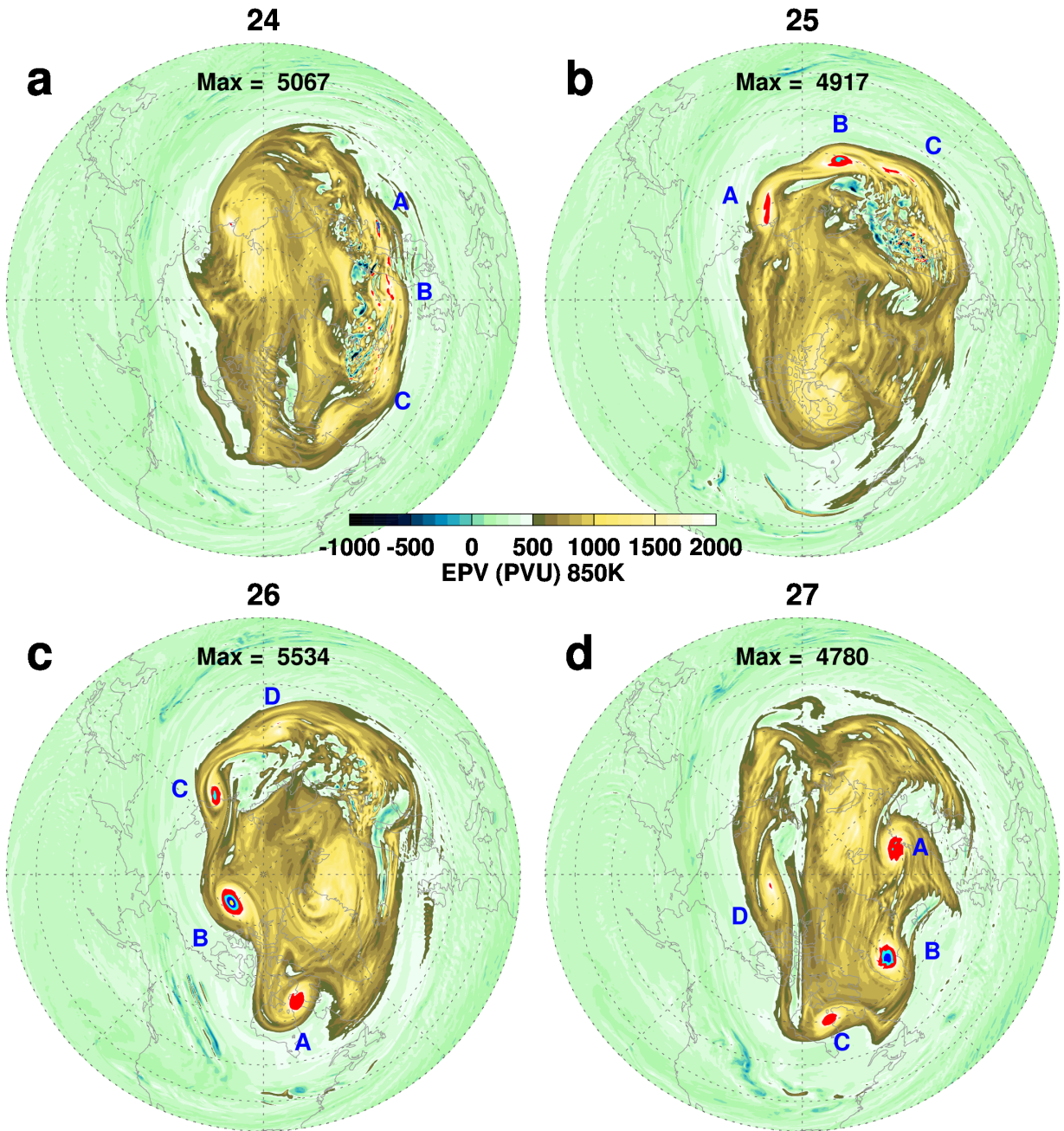
252 GW breaking. Much higher vertical and horizontal resolution simulations are needed to accurately
253 model the GW breaking process and its effect on EPV.

254 *c. mesoscale Vortices*

255 The mesoscale vortices develop and propagate along the edge of the vortex, just poleward of the
256 edge value delineating the low and high EPV regions. An example of the growth and propagation of
257 the mesoscale vortices from 24–27 January is shown in figure 9. EPV undulations, identified by the
258 letters, A, B, and C can be seen on 24 January (Fig. 9a) in a region of EPV that has separated from
259 the main high EPV region by gravity wave breaking (EPV fluctuations at the smallest resolvable
260 scale) from Greenland to Northern Europe. By 25 January (Fig. 9b), the three mesoscale vortices
261 have propagated about 90° in longitude around the main vortex. After crossing the main breaking
262 GW region the mesoscale vortices have increased in amplitude, moving in response to the larger
263 EPV values of the polar vortex. The mesoscale vortices, A, B, and C continue to increase in
264 amplitude (the value of their central EPV) on the 26 January (Fig. 9c) and there is also at this time
265 the identification of an additional trailing EPV region labeled D. On the last day shown, 27 January
266 (Fig. 9d), the mesoscale vortices continue their eastward propagation with A and D increasing in
267 amplitude while B and C decrease slightly in amplitude. Note that some of the mesoscale vortices
268 are associated with “breaking wave” signatures in the EPV field: A in panel c), and A, B, and C,
269 in panel d). In each of these mesoscale vortices EPV from the main vortex is being pulled off and
270 lower EPV mixed into the main vortex.

274 The trajectory of the mesoscale vortex B carried it nearly twice around the main vortex (Fig. 10).
275 After ~ 2 days increasing in strength (24–26 January), mesoscale vortex B kept its amplitude nearly
276 constant until ~ 28 January before weakening and crossing over the North Pole on 29 January and
277 eventually dissipating near Northern Europe. Mesoscale vortex B existed for about seven days
278 making its average period for a circulation around the globe approximately three and half days,
279 implying a propagation speed of 45 ms^{-1} at 70°N . This speed is close to the mean polar vortex
280 speed at this time, indicating that mesoscale vortex B has a well-conserved EPV structure during
281 this time.

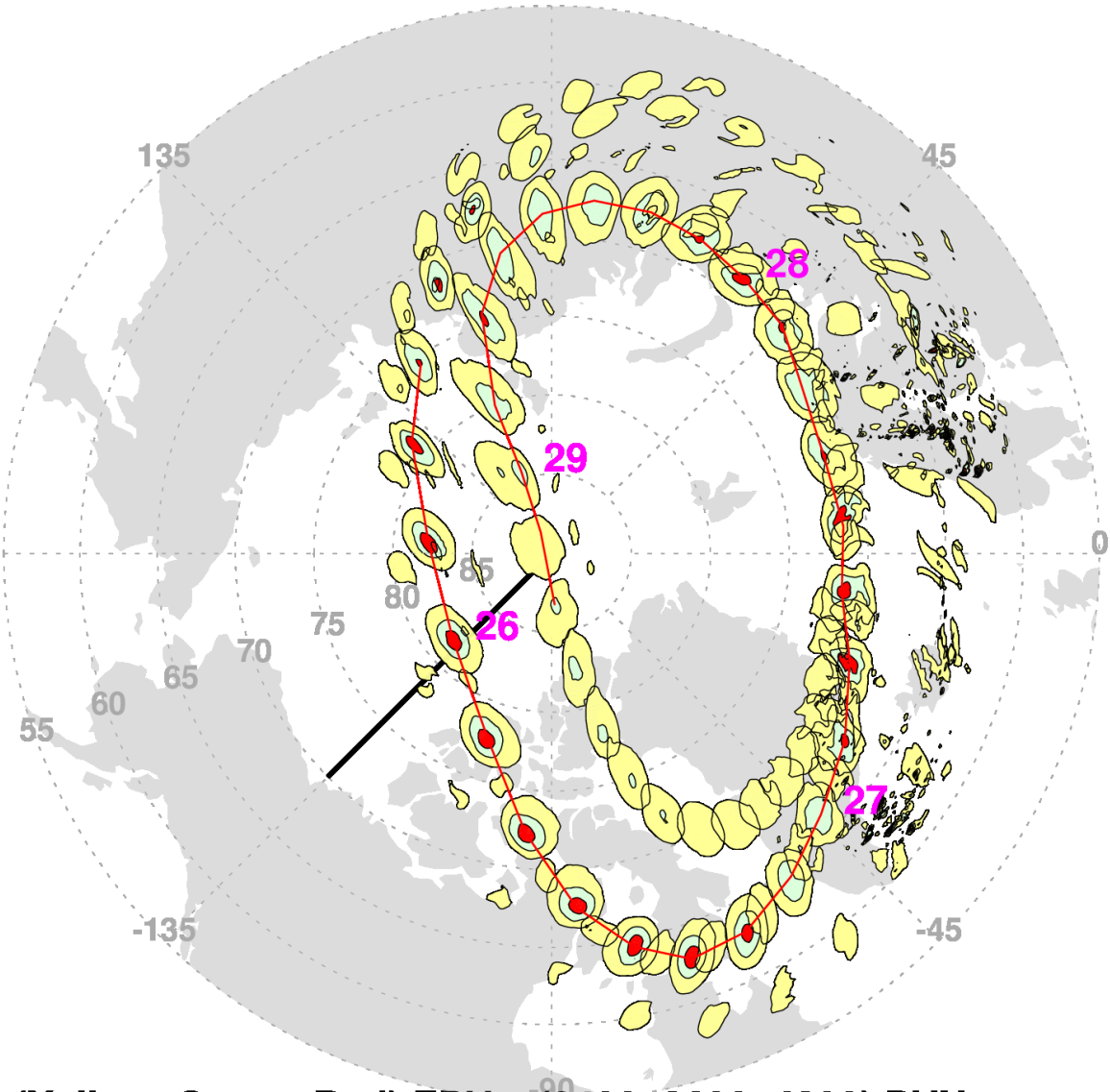
287 Cross sections of mesoscale vortex B on 26 January highlight typical vertical structure of the
288 mesoscale vortices during their largest amplitude (Fig. 11). The EPV anomaly extends from ~ 10 –



271 FIG. 9. EPV on 850K potential temperature surface for a) 24, b) 25, c) 26, and d) 27 January 2002 00UTC.
 272 The high EPV values are: red: 2000–3000 PVU, cyan: 3000–4000 PVU, blue: 4000–5000 PVU, and yellow:
 273 above 5000 PVU. Features tracked across panels are labeled A, B, C, and D.

289 1.5 hPa in the upper stratosphere while the potential temperature shows large perturbations starting
 290 just above 20 hPa and extending through the upper stratosphere. The temperature perturbation field

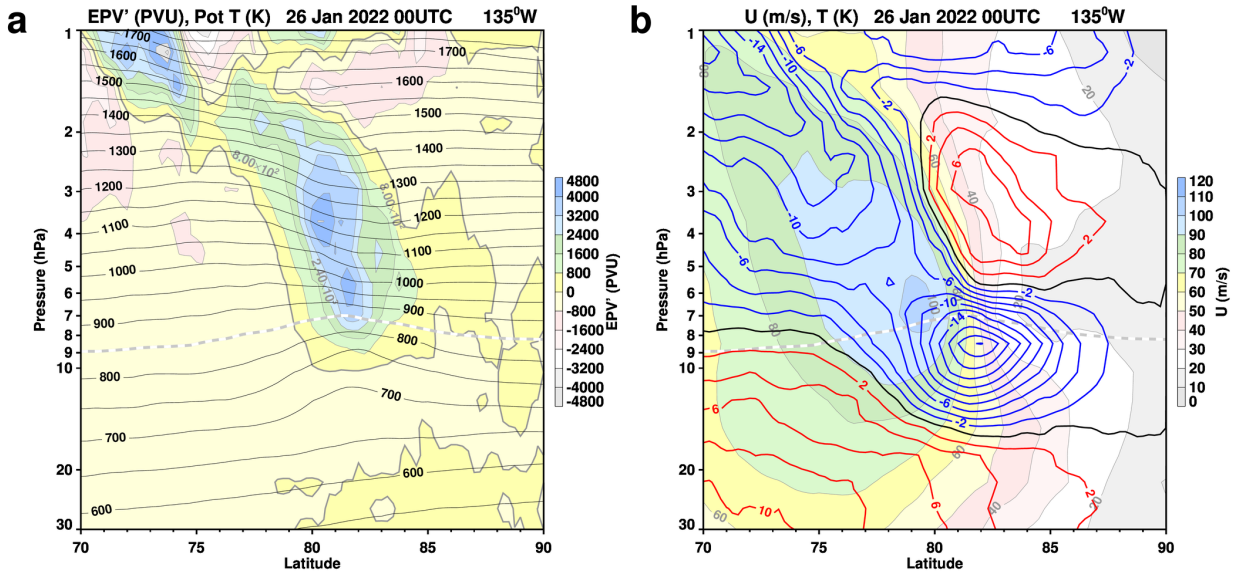
EPV 850K 24-31 Jan 2022



(Yellow, Green, Red) EPV > (2400, 3600, 4800) PVU

282 FIG. 10. EPV on the 850K potential temperature surface for 24–31 January 2022 contoured every three hours.
283 EPV values are colored between 2400–3600 PVU (yellow), 3600–4800 PVU (green), and greater than 4800 PVU
284 (red). The red curve connects the maximum EPV locations from 25 January 15 UTC to 29 January 6 UTC. The
285 locations of the highest EPV at 0 UTC on 26, 27, 28, and 29 January are marked. The black line denotes the
286 location of the cross section shown in Fig. 11.

291 is consistent with the potential temperature field with cool air below and warm air above. The wind
292 anomalies are located south and north of the axis of the temperature perturbation consistent with

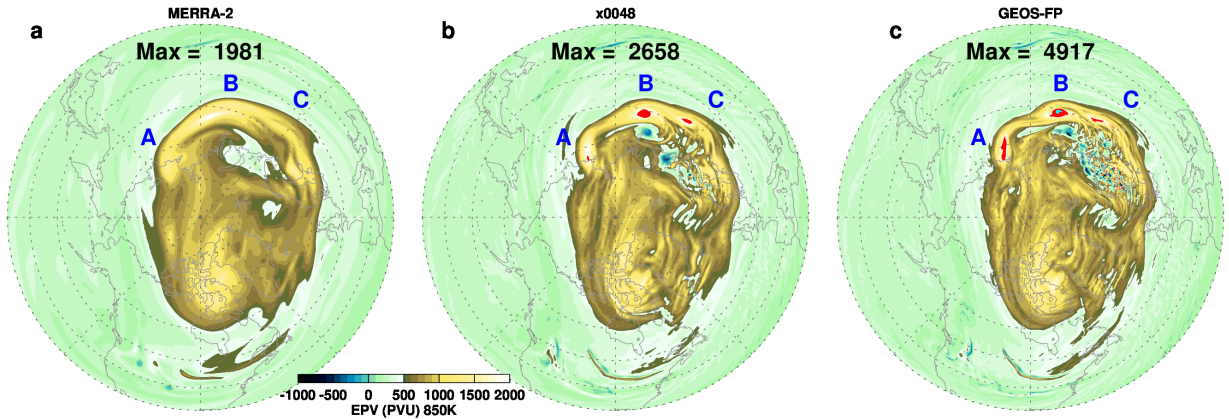


297 FIG. 11. Latitude (70° – 90° N) pressure (30–1 hPa) cross section at 135° W of a) EPV deviation from the
 298 zonal mean (PVU, filled contours) and potential temperature (K, black contours) and b) zonal wind (ms^{-1} , filled
 299 contours) and temperature deviation from the zonal mean (K, red positive, blue negative). The dashed gray curve
 300 denotes the 850K potential temperature.

293 the cyclonic circulation of the EPV anomalies. The strongest wind gradients (in the horizontal)
 294 coincide with the strongest temperature gradients (in the vertical). The wind change across the
 295 mesoscale vortex is $\sim 80 \text{ ms}^{-1}$. The mesoscale vortices are located in the upper stratosphere with
 296 little extent into the lower stratosphere.

301 *d. Resolution*

302 High horizontal resolution is needed to identify the breaking GW signature and to reveal the
 303 detailed structure of the mesoscale vortices. Figure 12 shows the 850 K potential temperature
 304 surface EPV field at $\sim 1/2$, $1/4$, and $1/8$ degree resolution (low, intermediate, and high). At the
 305 lowest resolution, there is no evidence of breaking GWs and while there is some appearance of the
 306 EPV fluctuations at the intermediate resolution, they are much more evident at the high resolution.
 307 The well-defined mesoscale vortices only appear at the intermediate and high resolution and have
 308 the highest central EPV values at high resolution. All three resolutions, even the lowest, capture
 309 the strong EPV region near A, B, and C, separated from the main vortex, creating a reversal in the
 310 latitudinal EPV gradient.



311 FIG. 12. EPV on 850K potential temperature surface for GEOS DAS analyses at three horizontal resolutions
 312 with nominal values of a) 1/2, b) 1/4, and c) 1/8 degrees on 25 January 2022 00UTC. Contours are the same as
 313 in Fig. 9

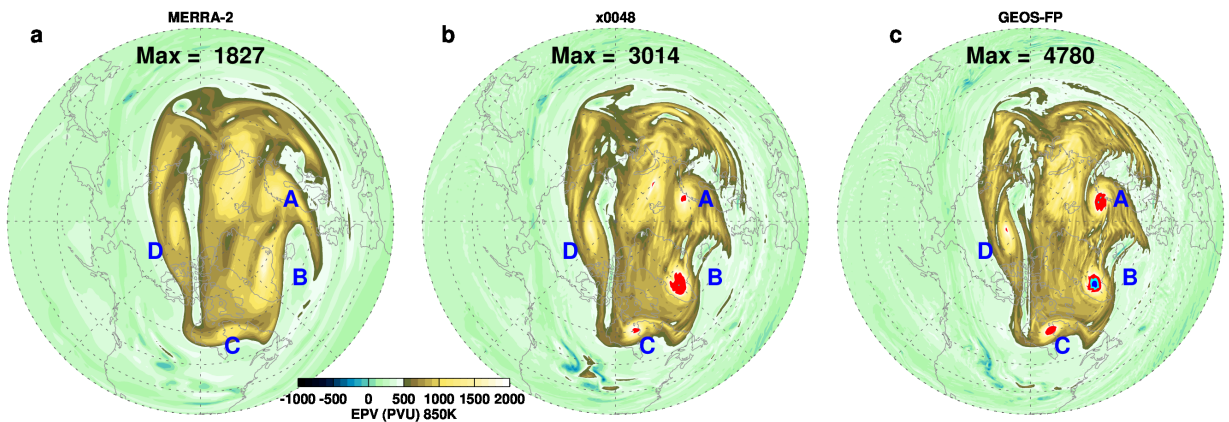


FIG. 13. Same as Fig. 12 but for 27 January 2022 00UTC

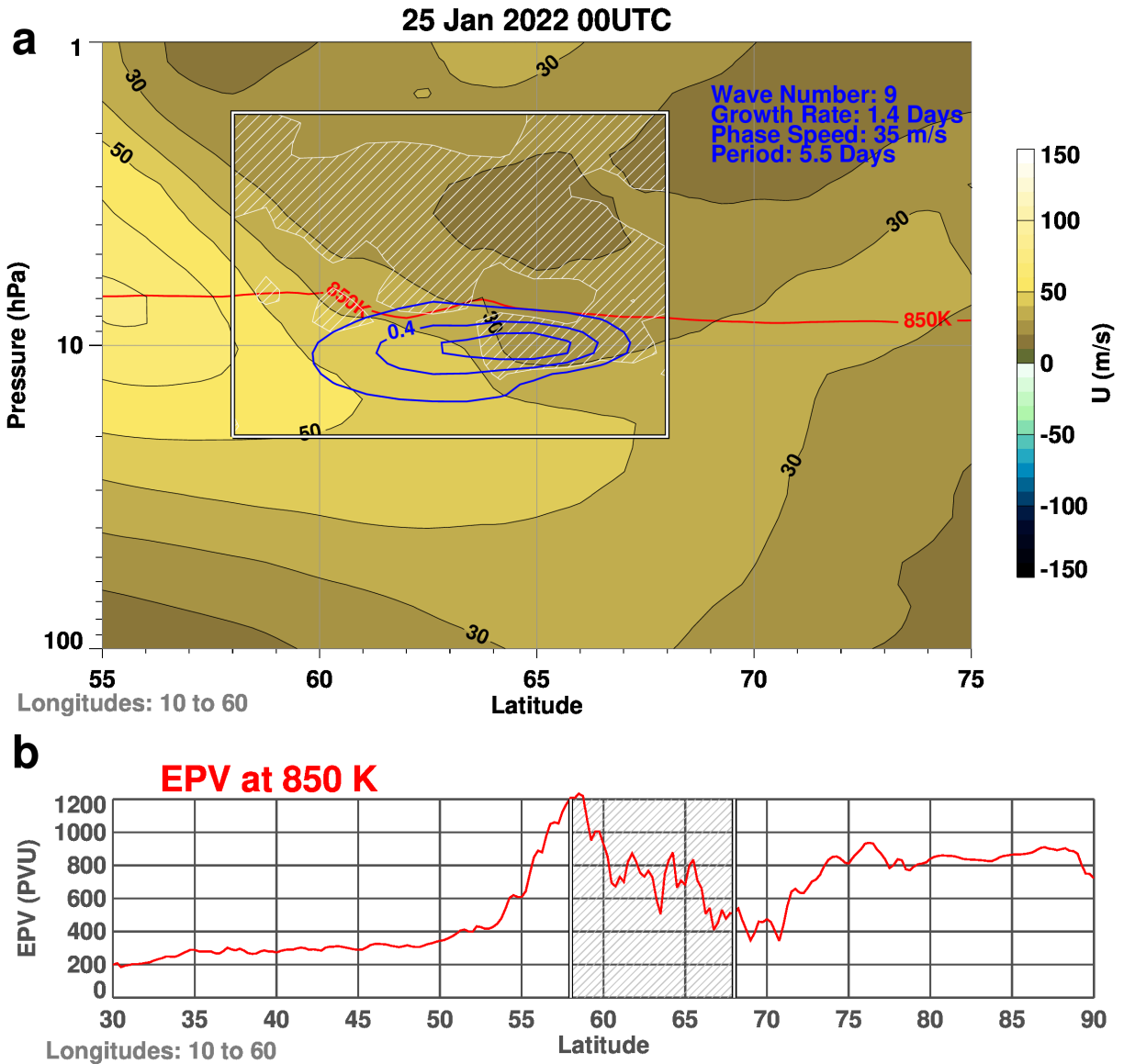
314 Later, on the 27th, the mesoscale vortices have propagated along the main vortex edge as
 315 identified by the letters (Fig. 13). They are very faint but present at low resolution, however both
 316 the intermediate and high resolutions agree well suggesting that the size of mesoscale vortices are
 317 converging with resolution and may not change much in even higher resolution systems. While
 318 the overall structure of the mesoscale vortices are similar at intermediate and high resolution, the
 319 central peak EPV values are still larger at the high resolution. Note that the maximum EPV values,
 320 occurring at mesoscale vortex “B”, increase from 3,014 at intermediate to 4,780 PVU at high
 321 resolution.

322 *e. Instability Considerations*

323 The idea presented here is that the tropospheric generated GWs break in the stratosphere over
324 a substantial area, creating a significant disruption of the polar vortex EPV, in turn triggering
325 instabilities near the edge of the polar vortex. The instability then produces the mesoscale vortices.
326 As a simple test of the instability of the flow, a linear instability model was examine for different
327 zonal wind profiles and times. One result is shown in figure 14. Since the reversed EPV gradient is
328 localized, the zonal winds near the GW activity, 10° – 60° E, were average for the background state.
329 The time chosen was for 25 January as the wave perturbation, especially the perturbations labeled
330 C and D in figure 9, were still growing at that time. Other choices include time averaging of the
331 zonal winds or selecting a different longitude range. In addition the model evaluates instability
332 over a limited latitude and pressure range, here chosen to be 58° – 68° N and 20–2 hPa. As in
333 McCormack et al. (2014) the boundary conditions were simply taken to be zero at all boundaries
334 of the box. The interior of the box includes a region of negative \bar{q}_y (Fig. 14a) and a reversal of the
335 EPV gradient (Fig. 14b).

336 For the above choices the fastest growing unstable wave was found at wavenumber 9, with an
337 e-folding growth rate of 1.4 days, a phase speed of 35 ms^{-1} , and a period of 5.5 days. Examining the
338 spacing of the mesoscale vortex locations of 25 January (Fig. 9b), the wavenumber 9 result is not
339 unrealistic, however the spacing between the mesoscale vortices does increase with time (Fig. 9d)
340 suggesting a smaller wavenumber. The growth rate is reasonable, however the phase speed appears
341 to be somewhat slow, leading to a period that is longer than observed when compared to the just
342 over 3-day circuit of the globe taken by the mesoscale vortex B (Fig. 9) from 26–29 January
343 (Fig. 10). The amplitude structure is confined to the lower region of the model’s domain in contrast
344 to the larger vertical extent seen in figure 11. Overall, the instability model results, while not
345 comprehensive, illustrate the potential for instability created by the breaking GW induced reversal
346 in the local EPV latitudinal gradient.

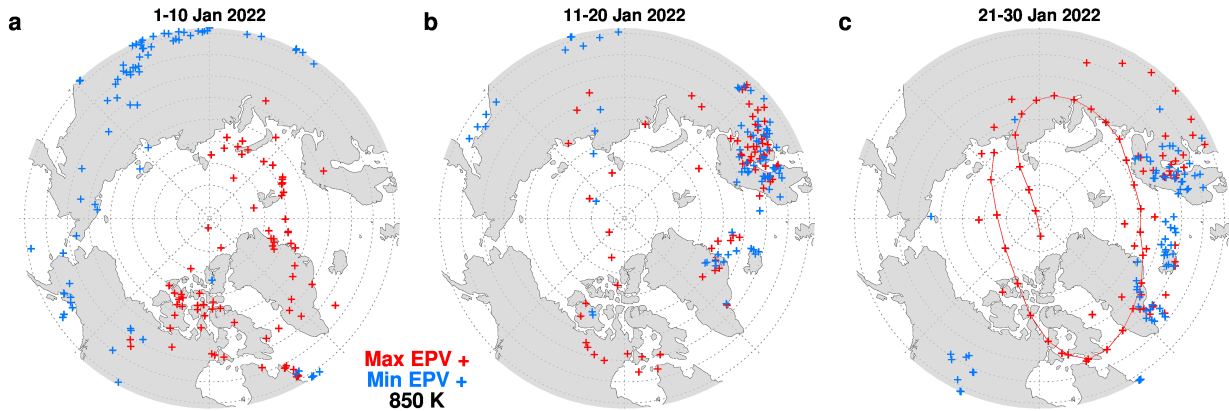
347 Note that this instability model cannot reproduced the observed growth in EPV as no diabatic
348 processes are included. In the this simple model, the EPV is rearranged to correspond to the growing
349 amplitude wave. The finite amplitude behavior of the instability requires a more sophisticated
350 model.



351 FIG. 14. a) zonal mean wind averaged over 10–60° E (filled contours), the region of negative \bar{q}_y (shaded), the
 352 850K potential temperature (red contour), the non-dimensional fastest growing wave amplitude (blue contours),
 353 and b) EPV (PVU) averaged over 10–60° E as a function of latitude. The box in a) and the shaded region in b)
 354 denotes the stability model domain used

355 4. Summary and Conclusions

356 This study based on the 12 km resolution DAS revealed two new features in the EPV analysis:
 357 high and low fluctuations at the smallest model scale associated with GW breaking, and high values
 358 associated with mesoscale vortices along the edge of the polar vortex. In this case both types of

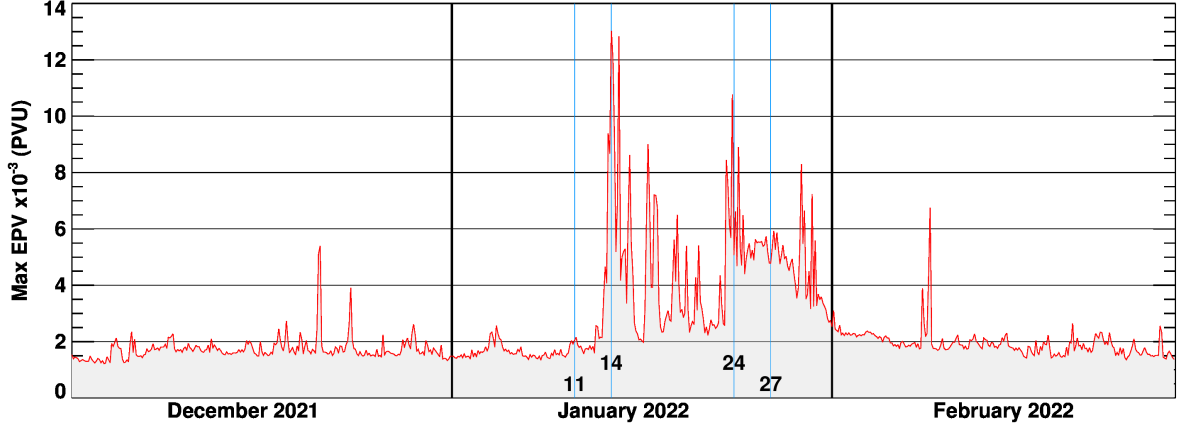


370 FIG. 15. The locations of the maximum (red) and minimum (blue) values of EPV on the 850K potential
 371 temperature surface at each analysis time for a) 1–10, b) 11–20, and c) 21–30 January 2022. The minimum
 372 locations are restricted to the area shown on the map projection. The red curve connects the maximum EPV
 373 locations from 25 January 15 UTC to 29 January 9 UTC.

359 anomalous EPV values were related, as the persistent GW breaking created a region of reversed
 360 EPV gradient that triggered the formation of the mesoscale vortices.

361 The location of NH maximum and minimum values of 850K EPV at each analysis time provides
 362 a convenient overview of the breaking GW regions during January 2022 (Fig. 15). During the
 363 first ten-days the highest EPV values are at the highest latitudes and lowest EPV values are at the
 364 lower latitudes, consistent with the NH climatological poleward gradient of EPV. By the middle of
 365 January, however, the distribution has changed with maximum and minimum EPV locations close
 366 together over Northern Europe, the Greenland coast, and Iceland. These indicate regions of strong
 367 GW breaking as seen in the EPV field. Later in January, these "salt and pepper" patterns continue
 368 with the addition of several days (25–29 January) when the maximum EPV value was associated
 369 with a propagating mesoscale vortex.

374 The maximum value of 850K EPV can characterized the overall NH winter of 2021–22 with a
 375 nominal maximum value of just under 2000 PVU for most of the winter season (Fig. 16). Starting
 376 on 14 January, values that are 5× higher appear, coincident with the appearance of GW breaking.
 377 These spikes continue for the remainder of the month with the addition of a more consistent in
 378 time bulge of high EPV, a signature of the persistent mesoscale vortices. These dramatic events
 379 are mostly over by the start of February.



380 FIG. 16. Maximum EPV value on the 850K potential temperature surface as a function of time (10^{-3} PVU).
 381 11, 14, 24, and 27 January 2022 are denoted by blue vertical lines.

382 How realistic are these very high EPV values seen in DAS? It is difficult to be definitive at this
 383 time. The very smallest scale EPV fluctuations, occurring in association with GW breaking, are
 384 likely greatly influence by the limited model resolution. However, higher horizontal resolution leads
 385 to more sharply defined mesoscale vortices with higher central EPV values (Fig. 13). Comparison
 386 of the evolution of the mesoscale vortices in FP with the lower resolution MERRA-2 EPV fields
 387 (Fig. 13) shows that at lower resolution the FP mesoscale vortices can be identified as a smoothed
 388 version of the higher resolution system. If the wind change is approximately the same across a
 389 mesoscale vortex but the doubled horizontal resolution allows for a doubling of the gradient, then
 390 the EPV values can be expected to double as well.

391 The creation of the very high mesoscale vortex EPV values is left for future investigation. In
 392 isentropic coordinates the rate of change of the parcel EPV is given by (Andrews et al. 1987,
 393 Equ 3.8.5):

$$\tilde{D}P = (\sigma a \cos \phi)^{-1} [-(X \cos \phi)_\phi + Y_\lambda - Q_\lambda v_\theta + Q_\phi u_\theta \cos \phi] + PQ_\theta - QP_\theta,$$

394 where \tilde{D} is the time derivative following the isentropic flow, P is potential vorticity, σ is the
 395 isentropic density, a is the radius of the earth, ϕ is latitude, λ is longitude, θ is potential temperature,
 396 X and Y are the latitude and longitude frictional forces, u and v are the velocity components, and

397 Q is the diabatic forcing. Neglecting frictional forces and scaling for quasi-geostrophic motion
398 (Haynes and McIntyre 1987), the equation becomes:

$$\tilde{D}P \approx PQ_\theta - QP_\theta$$

399 While time averaged diabatic heating terms are typically saved in the DAS output, the quadratic
400 terms are not save so additional output would be useful. In addition, the non-geostropic terms
401 may contribute to the mesoscale vortices. Along with the mesoscale high EPV, some regions of
402 mesoscale low EPV stand out. This is especially noticeable in Fig. 12b, the intermediate resolution
403 experiment, near “B” and “C”, suggesting that isentropic redistribution of EPV is playing a role
404 rather than problematic model numerics in creating the high EPV features.

405 The different orientation and scale of EPV fluctuations from the associated GWs needs further
406 investigation. Detailed three dimensional models of GW breaking (Fritts et al. 2009a,b) resolve
407 the small scale, rapid, variability created during the breaking process and the generation of EPV
408 by breaking GWs has been recently modeled by Waite and Richardson (2023). These studies
409 suggest that “spanwise”, that is disturbances along the wavefront, commonly develop, however
410 relating these to global scale EPV is not yet clear. While we have focused on a single NH winter
411 in which planetary wave activity was relatively weak to highlight the GWs and their effects on the
412 polar vortex, it is likely that breaking GWs in the mid to upper stratosphere are fairly common and
413 routinely contribute to mixing at the edge of the polar vortex.

414 In future studies we plan to examine other years when high resolution FP DAS fields are available
415 along with results from test model and assimilation experiments at higher horizontal and vertical
416 resolution. More evaluation of the amount of mixing along the polar vortex edge by the mesoscale
417 vortices is also needed. Even though the scale of these vortices is relatively small, the amount of
418 mixing could be substantial as these mesoscale vortices form where tracer gradients are large. In
419 addition, since some evidence of the mesoscale vortices can be found at low resolution such as
420 in Fig. 13a, it may be possible to develop a climatology of when these events occur by searching
421 the longer time record of the lower resolution MERRA-2 DAS. Such a climatology would provide
422 information of the role played by the mesoscale vortices in observed climatological stratospheric
423 tracer distributions.

424 *Acknowledgments.* his work was supported by NASA MAP (Grant NNG17HP01C) and ACPMAP
425 programs (Grants 80NSSC19K1005, NNH18ZDA001N). Resources supporting this work were
426 provided by the NASA High-End Computing (HEC) Program through the NASA Center for
427 Climate Simulation (NCCS) at Goddard Space Flight Center.

428 *Data availability statement.* The GEOS data used in this study/project have been provided by
429 the Global Modeling and Assimilation Office (GMAO) at NASA Goddard Space Flight Cen-
430 ter. The Forward Processing (FP) DAS output are archived at <https://portal.nccs.nasa.gov/datashare/gmao/geos-fp/das> and the system used in this study is labeled f5271_fp.
431 The MERRA-2 data is available from the NASA's Goddard Earth Sciences Data and In-
432 formation Services Center (GES DISC, <https://disc.gsfc.nasa.gov/datasets?project=MERRA-2>).
433 Specific MERRA-2 data sets used are contained in the references. The AIRS brightness
434 temperatures are available from https://datapub.fz-juelich.de/slcs/airs/gravity_waves/html/view_2022_014.html The IDL (Interactive Data Language) code used for the
435 quasi-geostrophic instability model is archived at https://gmao.gsfc.nasa.gov/gmaoftp/larrycoy/instability_code/stability_package.pro. The x0048 DAS fields used to
436 construct intermediate resolution EPV fields on 25 and 27 January 2022 are archived at
437 https://gmao.gsfc.nasa.gov/gmaoftp/larrycoy/mesoscale_vortices.

441 **References**

442 Alexander, M. J., 2010: Gravity waves in the stratosphere. *The Stratosphere: Dynamics, Transport,*
443 *and Chemistry*, L. M. Polvani, A. H. Sobel, and D. W. Waugh, Eds., American Geophysical
444 Union, Washington, DC, 109–122.

445 Andrews, D. G., J. R. Holton, and C. B. Leovy, 1987: *Middle Atmosphere Dynamics*. Academic
446 Press, 489 pp.

447 Arnold, N. P., W. M. Putman, and S. R. Freitas, 2020: Impact of resolution and parameterized
448 convection on the diurnal cycle of precipitation in a global nonhydrostatic model. *Journal of*
449 *the Meteorological Society of Japan. Ser. II*, **98** (6), 1279–1304, <https://doi.org/10.2151/jmsj.2020-066>.

451 Butchart, N., 2022: The stratosphere: a review of the dynamics and variability. *Weather and*
452 *Climate Dynamics*, **3** (4), 1237–1272, <https://doi.org/10.5194/wcd-3-1237-2022>, URL <https://wcd.copernicus.org/articles/3/1237/2022/>.

454 Fritts, D. C., and M. J. Alexander, 2003: Gravity wave dynamics and effects
455 in the middle atmosphere. *Reviews of Geophysics*, **41** (1), <https://doi.org/https://doi.org/10.1029/2001RG000106>, URL <https://agupubs.onlinelibrary.wiley.com/doi/abs/10.1029/2001RG000106>, <https://agupubs.onlinelibrary.wiley.com/doi/pdf/10.1029/2001RG000106>.

458 Fritts, D. C., L. Wang, J. Werne, T. Lund, and K. Wan, 2009a: Gravity wave instability dynamics
459 at high reynolds numbers. part i: Wave field evolution at large amplitudes and high frequencies.
460 *Journal of the Atmospheric Sciences*, **66** (5), 1126 – 1148, <https://doi.org/https://doi.org/10.1175/2008JAS2726.1>, URL <https://journals.ametsoc.org/view/journals/atsc/66/5/2008jas2726.1.xml>.

462 Fritts, D. C., L. Wang, J. Werne, T. Lund, and K. Wan, 2009b: Gravity wave instability dynamics at
463 high reynolds numbers. part ii: Turbulence evolution, structure, and anisotropy. *Journal of the At-*
464 *mospheric Sciences*, **66** (5), 1149 – 1171, <https://doi.org/https://doi.org/10.1175/2008JAS2727.1>, URL <https://journals.ametsoc.org/view/journals/atsc/66/5/2008jas2727.1.xml>.

466 Gelaro, R., and Coauthors, 2017: The Modern-Era Retrospective Analysis for Research and
467 Applications, Version 2 (MERRA-2). *Journal of Climate*, **30** (14), 5419–5454, <https://doi.org/10.1175/JCLI-D-16-0758.1>, URL <https://doi.org/10.1175/JCLI-D-16-0758.1>, <https://doi.org/10.1175/JCLI-D-16-0758.1>.

470 GMAO, 2015a: Global Modeling and Assimilation Office, inst3 3d asm Nv: MERRA-2 3D Assim-
471 ilated Meteorological Fields 3-hourly (model level, 0.625x0.5L42), version 5.12.4. Greenbelt,
472 MD, USA: Goddard Space Flight Center Distributed Active Archive Center (GSFC DAAC),
473 accessed June 2016, <https://doi.org/10.5067/WWQSQ8IVFW8>.

474 GMAO, 2015b: Global Modeling and Assimilation Office, instM 3d asm Np: MERRA-2 3D
475 IAU State, Meteorology Monthly Averaged 3-hourly (p-coord, 0.625x0.5L42), version 5.12.4.
476 Greenbelt, MD, USA: Goddard Space Flight Center Distributed Active Archive Center (GSFC
477 DAAC), accessed June 2016, <https://doi.org/10.5067/2E096JV59PK7>.

478 Haynes, P. H., and M. E. McIntyre, 1987: On the evolution of vorticity and potential vorticity
479 in the presence of diabatic heating and frictional or other forces. *Journal of Atmospheric Sci-*
480 *ences*, **44** (5), 828 – 841, [https://doi.org/https://doi.org/10.1175/1520-0469\(1987\)044<0828:](https://doi.org/https://doi.org/10.1175/1520-0469(1987)044<0828:)
481 [OTEOVA>2.0.CO;2](https://doi.org/https://doi.org/10.1175/1520-0469(1987)044<0828:), URL https://journals.ametsoc.org/view/journals/atsc/44/5/1520-0469_
482 [1987_044_0828_oteova_2_0_co_2.xml](https://journals.ametsoc.org/view/journals/atsc/44/5/1520-0469_1987_044_0828_oteova_2_0_co_2.xml).

483 Haynes, P. H., and M. E. McIntyre, 1990: On the conservation and impermeability theorems
484 for potential vorticity. *Journal of Atmospheric Sciences*, **47** (16), 2021 – 2031, [https://doi.org/](https://doi.org/https://doi.org/10.1175/1520-0469(1990)047<2021:OTCAIT>2.0.CO;2)
485 [https://doi.org/10.1175/1520-0469\(1990\)047<2021:OTCAIT>2.0.CO;2](https://doi.org/https://doi.org/10.1175/1520-0469(1990)047<2021:OTCAIT>2.0.CO;2), URL [https://journals.](https://journals.ametsoc.org/view/journals/atsc/47/16/1520-0469_1990_047_2021_otcait_2_0_co_2.xml)
486 [ametsoc.org/view/journals/atsc/47/16/1520-0469_1990_047_2021_otcait_2_0_co_2.xml](https://journals.ametsoc.org/view/journals/atsc/47/16/1520-0469_1990_047_2021_otcait_2_0_co_2.xml).

487 Hoffmann, L., M. J. Alexander, C. Clerbaux, A. W. Grimsdell, C. I. Meyer, T. Rößler, and
488 B. Tournier, 2014: Intercomparison of stratospheric gravity wave observations with AIRS
489 and IASI. *Atmospheric Measurement Techniques*, **7** (12), 4517–4537, [https://doi.org/10.5194/](https://doi.org/10.5194/amt-7-4517-2014)
490 [amt-7-4517-2014](https://doi.org/10.5194/amt-7-4517-2014), URL <https://amt.copernicus.org/articles/7/4517/2014/>.

491 Holt, L. A., M. J. Alexander, L. Coy, C. Liu, A. Molod, W. Putman, and S. Pawson, 2017: An eval-
492 uation of gravity waves and gravity wave sources in the southern hemisphere in a 7 km global cli-
493 mate simulation. *Quarterly Journal of the Royal Meteorological Society*, **143** (707), 2481–2495,
494 <https://doi.org/https://doi.org/10.1002/qj.3101>, URL [https://rmets.onlinelibrary.wiley.com/doi/](https://rmets.onlinelibrary.wiley.com/doi/abs/10.1002/qj.3101)
495 [abs/10.1002/qj.3101](https://rmets.onlinelibrary.wiley.com/doi/abs/10.1002/qj.3101), <https://rmets.onlinelibrary.wiley.com/doi/pdf/10.1002/qj.3101>.

496 Hoskins, B. J., M. E. McIntyre, and A. W. Robertson, 1985: On the use and significance
497 of isentropic potential vorticity maps. *Quarterly Journal of the Royal Meteorological Soci-*
498 *ety*, **111** (470), 877–946, <https://doi.org/https://doi.org/10.1002/qj.49711147002>, URL [https://](https://rmets.onlinelibrary.wiley.com/doi/abs/10.1002/qj.49711147002)
499 rmets.onlinelibrary.wiley.com/doi/abs/10.1002/qj.49711147002, [https://rmets.onlinelibrary.](https://rmets.onlinelibrary.wiley.com/doi/pdf/10.1002/qj.49711147002)
500 [wiley.com/doi/pdf/10.1002/qj.49711147002](https://rmets.onlinelibrary.wiley.com/doi/pdf/10.1002/qj.49711147002).

501 McCormack, J. P., L. Coy, and W. Singer, 2014: Intraseasonal and interannual variability
502 of the quasi 2 day wave in the northern hemisphere summer mesosphere. *Journal of Geo-*
503 *physical Research: Atmospheres*, **119** (6), 2928–2946, [https://doi.org/https://doi.org/10.1002/](https://doi.org/https://doi.org/10.1002/2013JD020199)
504 [2013JD020199](https://doi.org/https://doi.org/10.1002/2013JD020199), URL <https://agupubs.onlinelibrary.wiley.com/doi/abs/10.1002/2013JD020199>,
505 <https://agupubs.onlinelibrary.wiley.com/doi/pdf/10.1002/2013JD020199>.

- 506 McIntyre, M. E., and T. N. Palmer, 1983: Breaking planetary waves in the stratosphere. *Nature*,
507 **305**, 593–600.
- 508 Nash, E. R., P. A. Newman, J. E. Rosenfield, and M. R. Schoeberl, 1996: An objec-
509 tive determination of the polar vortex using ertel’s potential vorticity. *Journal of Geophys-*
510 *ical Research: Atmospheres*, **101 (D5)**, 9471–9478, [https://doi.org/https://doi.org/10.1029/](https://doi.org/https://doi.org/10.1029/96JD00066)
511 [96JD00066](https://doi.org/https://doi.org/10.1029/96JD00066), URL <https://agupubs.onlinelibrary.wiley.com/doi/abs/10.1029/96JD00066>, <https://agupubs.onlinelibrary.wiley.com/doi/pdf/10.1029/96JD00066>.
- 513 Okui, H., C. J. Wright, N. P. Hindley, E. J. Lear, and K. Sato, 2023: A comparison of stratospheric
514 gravity waves in a high-resolution general circulation model with 3-d satellite observations.
515 *Journal of Geophysical Research: Atmospheres*, **128 (13)**, e2023JD038795, [https://doi.org/](https://doi.org/https://doi.org/10.1029/2023JD038795)
516 [https://doi.org/10.1029/2023JD038795](https://doi.org/https://doi.org/10.1029/2023JD038795), URL [https://agupubs.onlinelibrary.wiley.com/doi/abs/](https://agupubs.onlinelibrary.wiley.com/doi/abs/10.1029/2023JD038795)
517 [10.1029/2023JD038795](https://agupubs.onlinelibrary.wiley.com/doi/abs/10.1029/2023JD038795), e2023JD038795 2023JD038795, <https://agupubs.onlinelibrary.wiley.com/doi/pdf/10.1029/2023JD038795>.
- 519 Putman, W. M., and S.-J. Lin, 2007: Finite-volume transport on various cubed-sphere grids.
520 *Journal of Computational Physics*, **227 (1)**, 55–78, [https://doi.org/https://doi.org/10.1016/j.jcp.](https://doi.org/https://doi.org/10.1016/j.jcp.2007.07.022)
521 [2007.07.022](https://doi.org/https://doi.org/10.1016/j.jcp.2007.07.022), URL <https://www.sciencedirect.com/science/article/pii/S0021999107003105>.
- 522 Shibuya, R., and K. Sato, 2019: A study of the dynamical characteristics of inertia–gravity
523 waves in the antarctic mesosphere combining the PANSY radar and a non-hydrostatic general
524 circulation model. *Atmospheric Chemistry and Physics*, **19 (5)**, 3395–3415, [https://doi.org/](https://doi.org/10.5194/acp-19-3395-2019)
525 [10.5194/acp-19-3395-2019](https://doi.org/10.5194/acp-19-3395-2019), URL <https://acp.copernicus.org/articles/19/3395/2019/>.
- 526 Stevens, B., and Coauthors, 2019: DYAMOND: the DYNAMics of the Atmospheric general
527 circulation Modeled On Non-hydrostatic Domains. *Prog Earth Planet Sci*, **6 (61)**, URL
528 <https://doi.org/10.1186/s40645-019-0304-z>.
- 529 Waite, M. L., and N. Richardson, 2023: Potential vorticity generation in breaking gravity
530 waves. *Atmosphere*, **14 (5)**, <https://doi.org/10.3390/atmos14050881>, URL <https://www.mdpi.com/2073-4433/14/5/881>.
- 532 Zhu, Y., R. Todling, and N. Arnold, 2022: Observation impact and information retention in
533 the lower troposphere of the gmao geos data assimilation system. *Monthly Weather Review*,

534 **150 (8)**, 2187 – 2205, <https://doi.org/https://doi.org/10.1175/MWR-D-21-0334.1>, URL [https:](https://journals.ametsoc.org/view/journals/mwre/150/8/MWR-D-21-0334.1.xml)
535 [//journals.ametsoc.org/view/journals/mwre/150/8/MWR-D-21-0334.1.xml](https://journals.ametsoc.org/view/journals/mwre/150/8/MWR-D-21-0334.1.xml).